

Machine Learning Identification of Gravimentally Microlensed Gamma-Ray Bursts

Mohammad H. Zhoolideh Haghighi^{*1,2}, Zeinab Kalantari^{†3}, Sohrab Rahvar^{4,5}, and Alaa Ibrahim⁶

¹Department of Physics, K.N. Toosi University of Technology, Tehran
P.O. Box 15875-4416, Iran

²School of Astronomy, Institute for Research in Fundamental Sciences
(IPM), Tehran, 19395-5746, Iran

³Research Center for High Energy Physics, Sharif University of
Technology, Tehran 11365-9161, Iran

⁴Department of Physics, Sharif University of Technology, Tehran
11365-9161, Iran

⁵Research Center for High Energy Physics, Sharif University of
Technology, Tehran 11365-9161, Iran

⁶Department of Physics, College of Science, P.O.Box 36, P.C. 123,
Muscat, Sultanate of Oman

April 29, 2025

Abstract

Gravitational microlensing of gamma-ray bursts (GRBs) provides a unique opportunity to probe compact dark matter and small-scale structures in the universe. However, identifying such microlensed GRBs within large datasets is a significant challenge. In this study, we develop a machine learning approach to distinguish Lensed GRBs from their Non-lensed counterparts using simulated light curves. A comprehensive dataset was generated, comprising labeled light curves for both categories. Features were extracted using the Cesium package, capturing critical temporal properties of the light curves. Multiple machine learning models were trained on the extracted features, with Random

^{*}zhoolideh@kntu.ac.ir

[†]zeinab.kalantari70@gmail.com

Forest achieving the best performance, delivering an accuracy of 94% and an F1 score of 95% (94%) for Non-Lensed (Lensed) class. This approach successfully demonstrates the potential of machine learning for identifying gravitational lensing in GRBs, paving the way for future observational applications.

Keywords: Machine learning – Astronomy data analysis – GRBs – Light Curves – Gravitational Lensing

1 Introduction

Gamma-ray bursts (GRBs) are among the most luminous transient events in the universe, originating from phenomena such as the collapse of massive stars or the merger of compact objects [24, 19]. Their fleeting nature and diverse temporal structures provide a wealth of information about the physical processes at play, but also pose significant challenges for analysis. Given the cosmological distances of GRBs, gravitational lensing offers a unique opportunity to explore the compact small-scale structures of the Universe, potentially revealing information about compact dark matter objects [27, 15]. Also, it provides a new tool for studying the cosmological models [16]. Theoretical studies on gravitational lensing of GRBs have been conducted for decades [30]. It has been proposed that GRBs can be gravitationally lensed, producing multiple images of the same burst. These images are observed as light curves arriving at different times due to variations in the light paths. In strong lensing, the time delay between images exceeds the burst duration. However, in microlensing, the time delay is shorter than the burst duration, causing the lensed images to appear as echoes within the same light curve. These echoes manifest as similar local peaks separated by the time delay, corresponding to unresolved lensed images ([29, 13, 14, 15, 17]). In this study, we utilized long gamma-ray bursts with durations of $T_{90} \geq 2$ seconds, observed by the Fermi Gamma-Ray Burst Monitor (GBM) ([23]), to simulate microlensed GRBs. Our focus is on lensing effects that generate two images, which appear as local peaks (or echoes) in the light curve. These peaks exhibit identical temporal variability but differ in magnification/flux and are separated by a time delay.

We use long GRBs (with $T_{90} \geq 2s$) data of the Fermi Gamma-Ray Burst Monitor (GBM) for simulating microlensed GRB ([23]). To model this, we performed Monte Carlo simulations using a point-mass lens model for mass within the range of $10^3 - 10^7 M_{\odot}$. This mass range was chosen because our analysis targeted time delays of less than 300 seconds. The time delay for

GRBs lensed by point masses is estimated to be related to the mass with the function $\Delta t = 50s \ M_L/10^6 M_\odot$ [22].

Identifying microlensed GRBs requires efficient methods for analyzing their light curves, as the lensing-induced features are often subtle and difficult to discern. Machine learning (ML) has revolutionized the analysis of complex datasets in various astrophysical domains and the rapid growth of astronomical data, combined with machine learning techniques, has significantly advanced the field of astronomy (see [2], [40], [38], [1], [41]) In time-domain astronomy, ML has been employed for tasks such as variable star classification [32], transient detection [25], and even anomaly detection in large-scale surveys [20]. These applications demonstrate the power of ML to extract meaningful patterns from noisy, high-dimensional data, making it a natural choice for analyzing GRB light curves.

Specifically, ML has shown great promise in GRB studies. Previous works have utilized ML to classify GRB types (long versus short bursts) [39], predict redshifts [18], and estimate spectral parameters [37]. The ability of ML to identify rare events, such as gravitationally lensed GRBs, is particularly valuable given the rarity of such phenomena and the vast amount of observational data produced by modern telescopes.

Feature extraction is a critical step in ML-based analysis of time-series data, such as GRB light curves. Tools like the **Cesium** package enable the automated extraction of relevant features, including temporal and frequency-domain properties, which are essential for distinguishing between Lensed and Non-lensed GRBs [26]. These features, when combined with robust classification algorithms such as Random Forests, can significantly enhance the accuracy of identifying microlensed GRBs. In this study, we aim to determine whether the presence of two local peaks in the light curve data of a GRB is due to gravitational lensing. Therefore, we create two datasets of mock Lensed and Non-lensed data, each containing 2000 light curves, and test different machine learning classifiers on our generated data. Features are extracted from these light curves using **Cesium**, capturing both statistical and physical characteristics. Multiple ML models are trained on the extracted features, and their performances are compared. The Random Forest algorithm achieves the highest accuracy of 94% and an F1 score of 95%, demonstrating its effectiveness in distinguishing gravitational microlensed GRBs.

This paper is structured as follows: In Section 2, we explain the physics of gravitational microlensing of GRBs. In Section 3, we describe the simulation of GRB light curves, the creation of our training and test sets, and feature extraction. Section 4 explains the machine learning methodologies

employed. Finally, Section 5 presents the classification results, compares the performance of different models, and discusses the implications of our findings.

2 Gravitational Microlensing

Gravitational lensing occurs when a massive object is positioned near the line of sight between an observer and a source. A point mass gravitational lens amplifies the source and produces two distinct images. In this study, a GRB serves as the source, and each image, influenced by gravitationally induced time delay and varying magnification, can be identified through the observed burst light curve.

Two key parameters in gravitational lensing play a crucial role in analyzing the GRB light curve. The first is the time delay between the two images, determined under the assumption of a point mass model for the lens. By defining the normalized impact parameter as $y = \frac{\beta}{\theta_E}$ where β represents the angular source position and θ_E the Einstein radius. The time delay can be calculated as described by [15].

$$\Delta t = t^+ - t^- = 4 \frac{GM_L}{c^3} (1 + z_L) \left[\frac{y}{2} \sqrt{y^2 + 4} + \ln \left(\frac{\sqrt{y^2 + 4} + y}{\sqrt{y^2 + 4} - y} \right) \right], \quad (1)$$

Here, M_L represents the lens mass, while $\Delta t = t^- - t^+$ denotes The relative time delay between fainter (negative parity) and brighter (positive parity) lensed images. The lens redshift is given by z_L .

The second key parameter is the flux ratio between the two images, which is determined by the ratio of their respective magnification factors [15].

$$R = \left| \frac{\mu_+}{\mu_-} \right| = \frac{y^2 + 2 + y\sqrt{y^2 + 4}}{y^2 + 2 - y\sqrt{y^2 + 4}}, \quad (2)$$

Here, μ_{\pm} represents the magnification factors of the positive and negative parity images. The time delay Δt is positive when $t^- \geq t^+$, meaning the fainter peak of the light curve, which corresponds to the image with the lower magnification, will arrive later than the brighter one, which corresponds to the image with the higher magnification (*i.e.* $t^+ \leq t^-$) as derived from Eqs. (1) and (2).

Assuming a lens mass of $5 \times 10^5 M_{\odot}$ and placing the lens at a cosmological redshift of approximately half the GRB's distance ($z_L = 1 \sim 1Gpc$), the

angular separation between the two images, $|\theta_+ - \theta_-|$, would be on the order of 10^{-2} arcseconds. The angular resolution of Fermi/GBM ($\sim 2^\circ$) is insufficient to distinguish between two gravitationally lensed images with small angular separations. However, lensing events with closely spaced images and shorter time delays can create detectable repeated structures or echoes with different magnifications within the same GRB light curve. As a result, the two gravitationally lensed images of a GRB would be observed as a single event, with the images manifesting as consecutive peaks or sub-bursts within the same light curve. This occurs when the time delay between the two images falls within the range where it is shorter than the total observation period but longer than the burst duration.

3 Data

We used data from the GBM instrument of the Fermi telescope to obtain the light curves of GRBs. Fermi/GBM records GRBs in a broad energy range (8 keV to 40 MeV) with a field of view of ≥ 8 sr and has twelve thallium-activated sodium iodide (NaI) and two bismuth germanate (BGO) detectors ([23]). For simulation, we extracted light curve data from the NaI detectors with the highest signal using the time-tagged event (TTE) files and considered long GRBs (with $T_{90} \geq 2s$) and then we subtract the background for a zeroth-order polynomial model (a constant) is chosen to fit the background. For performing a Monte Carlo simulation of mock lensed GRBs, we select 81 long GRBs from the Fermi/GBM catalog [36] that have one pulse in their light curves with a time bin of 64 ms. In the section 3.1 we illustrate how we produced mock microlensed light curves of these GRBs by imposing a time delay and a magnification factor for the lensed mass resulting from solving gravitational lensing equations that are mentioned in section 2. In the following section, we aim to identify whether the presence of two local peaks in the light curve of a GRB is a result of gravitational lensing. To achieve this, we generate two datasets—one with mock lensed data and another with non-lensed data.

3.1 Simulations

While the sub-arcsecond angular separation of two images of a GRB lensed by the previously mentioned mass will not be resolved by Fermi, and the GRB will be recorded as a single event, the light curve recorded by Fermi/GBM will be a superposition of the two light curves corresponding to the two lensed

images. This can be resolved when the time delay is shorter than the GRB recording time.

We aim to generate a semi-synthetic dataset that incorporates original light curves derived from real data. Using our Monte Carlo simulation, we will classify the light curves into two categories: lensed and non-lensed.

- **Mock lensed light curve:** Based on the physics of gravitational microlensing, for a redshifted lens mass ($M_L(1+z)$) assumed uniformly distributed over the interval $10^3 - 10^7 M_\odot$ and a normalized impact parameter uniformly distributed within $\beta = [0, 1]$, we first solve the lensing equations (Eq(1) and Eq(2)) to find time delay Δt and a magnification ratio R . Then we simulated a lensed light curve by superimposing the count rate $I(t)$ of a real GRB with itself as shown in Fig.1(Left), by imposing a time delay Δt and a magnification ratio R . The resulting lensed light curve count rate is

$$I_{Lensed}(t) = \frac{R}{R+1}I(t) + \frac{1}{R+1}I(t + \Delta t). \quad (3)$$

The crucial feature of the simulation of lensed light curves is that two local pulses in the GRB light should have the same temporal profile, separated by a time interval. So both count rates of the simulated lensed light curve are chosen from the same GRB light curve.

- **Mock Non-lensed light curve:** For the non-lensed simulation, we generate a light curve pattern with two local peaks, where the fainter peak occurs later than the brighter one, but each peak exhibits a distinct temporal profile. Therefore, we superimpose the count rate $I(t)$ of a real GRB (for the brighter peak) with another GRB's light curve $I'(t)$ (for the second peak), as shown in Fig.1 (right). This is done by introducing a randomly chosen time delay Δt and an amplification factor, A , to ensure that the fainter peak appears later than the brighter one. The resulting light curve count rate is:

$$I_{Non-lensed}(t) = AI(t) + I'(t + \Delta t). \quad (4)$$

The main feature of the simulation of the Non-lensed light curve is that the two pulse shapes are different, and we choose the second peak data from another GRB light curve.

Based on the method explained above, we simulate 4000 light curves, including 2000 Lensed and 2000 Non-Lensed GRBs. We extract the

important features of the generated light curves below, which will serve for training the machine learning models.

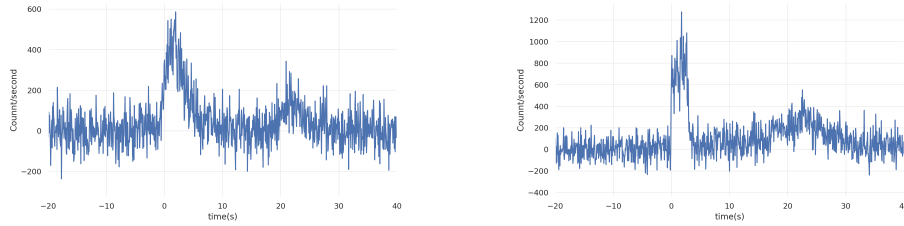


Figure 1: left: simulated Lensed light curve (see Eq.(3)). Right: simulated Non-lensed light curve (see Eq.(4))

3.2 Feature Selection and Extraction

To detect gravitational microlensed gamma-ray bursts (GRBs), we extracted a set of statistical and temporal features from the light curves of GRBs. These features were chosen based on their ability to capture the underlying characteristics of the light curves, which are critical for distinguishing microlensed GRBs from non-microlensed ones. The features were computed using the `cesium` feature extraction package [6], which provides a comprehensive suite of tools for time-series analysis in astrophysics.

The following features were extracted from the light curves:

- **Amplitude:** Measures the range of variability in the light curve count rate.
- **Percent Beyond 1 Std:** Quantifies the fraction of data points beyond one standard deviation from the mean.
- **Maximum, Minimum, and Median:** Capture the extreme values and central tendency of the light curve.
- **Skew:** Measures the asymmetry of the light curve distribution.
- **Maximum Slope:** This feature quantifies the steepest slope observed in the light curve, which is indicative of rapid changes in brightness.
- **Percentage Beyond 1 Standard Deviation:** This feature measures the proportion of data points in the light curve that lie beyond one standard deviation from the mean.

- **Standard Deviation (Std):** Represents the variability in the light curve.
- **Weighted Average:** Computes the mean weighted by measurement uncertainties.
- **Anderson-Darling and Shapiro-Wilk:** Statistical tests for normality, which help identify deviations from Gaussian behavior.
- **Stetson J and K:** Measures of variability and correlation in time-series data [35].
- **Median Absolute Deviation (MAD):** A robust measure of dispersion.
- **Percent Close to Median:** Quantifies the fraction of data points near the median value.
- **Period Fast:** Estimates the dominant periodicity in the light curve.
- **QSO Log Chi-Squared Features:** Derived from quasar variability studies, these features are useful for characterizing non-periodic variability [21].
- **Number of Peaks and Epochs:** Captures the structure and sampling of the light curve.

These features were selected based on their demonstrated effectiveness in characterizing astronomical time-series data [33, 10]. The feature extraction process was performed using the `featurize_time_series` function from the `cesium` package, which outputs a feature matrix \mathbf{X} where each row corresponds to a GRB and each column represents a feature.

The extracted features will be used as input to a machine learning model for classification. The target variable \mathbf{y} consists of binary labels indicating whether a GRB is microlensed or not. We split the dataset into training and testing sets using an 80-20 split, ensuring that the model’s performance could be evaluated on unseen data.

The use of machine learning for detecting microlensed GRBs is motivated by the complexity and high dimensionality of the light curve data. Traditional methods often rely on manual inspection or simple thresholding techniques, which may fail to capture subtle signatures of microlensing [28]. By leveraging a diverse set of features and advanced machine learning algorithms, our approach aims to improve the accuracy and robustness of microlensed GRB detection.

4 Model definition & training

4.1 Machine Learning Models and Architecture

To detect gravitational microlensed gamma-ray bursts (GRBs), we employed a diverse set of machine learning classifiers, each chosen for its unique strengths in handling high-dimensional data and capturing complex patterns. The models used in this study include:

- **Random Forest (RandomForestClassifier):** An ensemble method that constructs multiple decision trees during training and outputs the mode of the classes for classification tasks [5]. Random Forest is robust to overfitting and provides feature importance rankings, which are useful for interpreting the results.
- **Bagging Classifier (BaggingClassifier):** An ensemble method that combines the predictions of multiple base classifiers trained on random subsets of the data [4]. Bagging reduces variance and improves generalization performance.
- **AdaBoostClassifier:** An ensemble learning algorithm that combines multiple weak classifiers to create a strong classifier by iteratively adjusting the weights of misclassified samples [11]. This method is particularly effective in reducing bias and variance, making it suitable for various classification tasks, including astronomy and astrophysics applications.
- **k-Nearest Neighbors (KNeighborsClassifier):** A non-parametric method that classifies data points based on the majority class among their k nearest neighbors [8]. This model is effective for capturing local patterns in the data.
- **Support Vector Classifier (SVC):** A kernel-based method that finds the optimal hyperplane to separate classes in a high-dimensional feature space [7]. SVC is particularly effective for datasets with clear margins of separation.
- **Logistic Regression:** A widely used statistical model for binary classification that predicts the probability of an instance belonging to a class using a logistic function. It is trained using maximum likelihood estimation and is known for its interpretability and efficiency [12]. Logistic Regression often serves as a strong baseline for evaluating more complex models due to its simplicity and robustness.

The diversity of the selected models ensures that both linear and non-linear relationships in the data are captured. By comparing the performance of these models, we aim to identify the most effective approach for detecting microlensed GRBs.

4.1.1 Model Evaluation

In classification tasks, predictions can result in four outcomes: *True Positives (TP)*, where an observation is correctly predicted to belong to a class; *True Negatives (TN)*, where an observation is correctly predicted not to belong to a class; *False Positives (FP)*, where an observation is incorrectly predicted to belong to a class; and *False Negatives (FN)*, where an observation is incorrectly predicted not to belong to a class. These outcomes are typically organized in a confusion matrix, which categorizes predictions made on test data.

Model performance is evaluated using metrics such as *accuracy*, *precision*, *recall*, and the *F₁ score*. Accuracy measures the proportion of correct predictions relative to the total number of predictions:

$$\text{Accuracy} = \frac{\text{correct predictions}}{\text{all predictions}}$$

Precision quantifies the fraction of true positives among all predicted positives:

$$\text{Precision} = \frac{\text{true positives}}{\text{true positives} + \text{false positives}}$$

Recall, or sensitivity, measures the fraction of true positives identified out of all actual positives:

$$\text{Recall} = \frac{\text{true positives}}{\text{true positives} + \text{false negatives}}$$

The *F₁ score* combines precision and recall into a single metric by calculating their harmonic mean, providing a balanced measure of classifier performance. A score of 1 indicates perfect classification, while lower values reflect poorer performance:

$$F_1 = \frac{2 \cdot \text{Precision} \cdot \text{Recall}}{\text{Precision} + \text{Recall}}$$

Additionally, the *Receiver Operating Characteristic (ROC) curve* is a graphical tool used to assess the performance of binary classifiers. It plots

the *True Positive Rate (TPR)* against the *False Positive Rate (FPR)* across varying classification thresholds. The *Area Under the Curve (AUC)* summarizes the classifier’s ability to distinguish between classes, with an AUC of 1 representing perfect discrimination and 0.5 indicating no better than random chance. ROC analysis is particularly valuable for imbalanced datasets, as it evaluates performance across different thresholds, offering a robust assessment of model efficacy [9, 31, 3, 34].

4.2 Model Training

To distinguish between micro-lensed and Non-lensed gamma-ray bursts (GRBs), we employed multiple machine learning classifiers. The models were trained using a dataset of extracted features from simulated GRB light curves. The training process involved fitting each classifier to the training set $(X_{\text{train}}, y_{\text{train}})$, and the performance was evaluated on a separate test set $(X_{\text{test}}, y_{\text{test}})$. The classifiers implemented include: Random Forest, Classifier (RF), Support Vector Machine (SVM), k-Nearest Neighbors (kNN), Bagging Classifier, Logistic Regression, AdaBoost Classifier (AdaBoost). Each classifier’s performance was assessed using a confusion matrix and classification report. Figure 2 presents the normalized confusion matrices for all six models, providing insights into their classification effectiveness.

Furthermore, Table 1 summarizes the classification performance metrics, including precision, recall, and F1-score for each model.

5 Results

5.1 Model Performance

In this section, we present the performance of various machine learning models trained on the dataset for classifying Lensed and Non-lensed objects. The evaluation metrics include precision, recall, F1-score, accuracy, and the Area Under the Curve (AUC) plotted in Figure 3. The results are summarized in Table 1 and discussed in detail below.

The results indicate that the *Random Forest (RF)* model outperforms all other models, achieving the highest accuracy of 94% and an exceptional AUC of 0.99. It also demonstrates strong performance across both classes, with an F1-score of 0.95 for non-lensed objects and 0.94 for lensed objects. This suggests that RF is robust and well-suited for this classification task.

The *Bagging Classifier* also performs well, achieving an accuracy of 92% and an AUC of 0.98. Its balanced F1-scores of 0.92 for both classes further

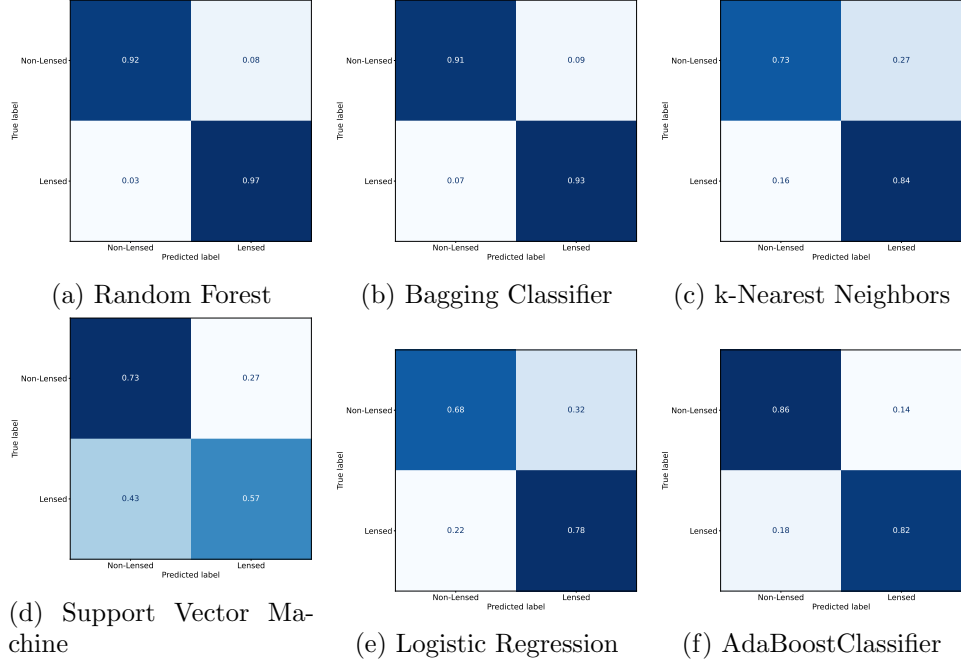


Figure 2: Normalized confusion matrices for six machine learning models used to classify Lensed and Non-lensed GRBs.

confirm its effectiveness. While slightly lower than RF, its performance is still competitive, indicating that ensemble methods are highly effective for this problem.

The *AdaBoostClassifier* achieves an accuracy of 84% and an AUC of 0.92, with F1-scores of 0.85 for non-lensed objects and 0.83 for lensed objects. Although its performance is lower than RF and Bagging, it still demonstrates reasonable capability in handling the classification task, particularly in terms of class separation.

The *k-Nearest Neighbors (kNN)* model achieves an accuracy of 78% and an AUC of 0.85, with F1-scores of 0.78 for non-lensed objects and 0.79 for lensed objects. While kNN performs adequately, its lower accuracy and F1-scores suggest that it may struggle with the complexity of the dataset. However, its AUC indicates moderate success in distinguishing between the two classes.

The *Logistic Regression* model achieves an accuracy of 69% and an AUC of 0.80, with F1-scores of 0.72 for non-lensed objects and 0.66 for lensed

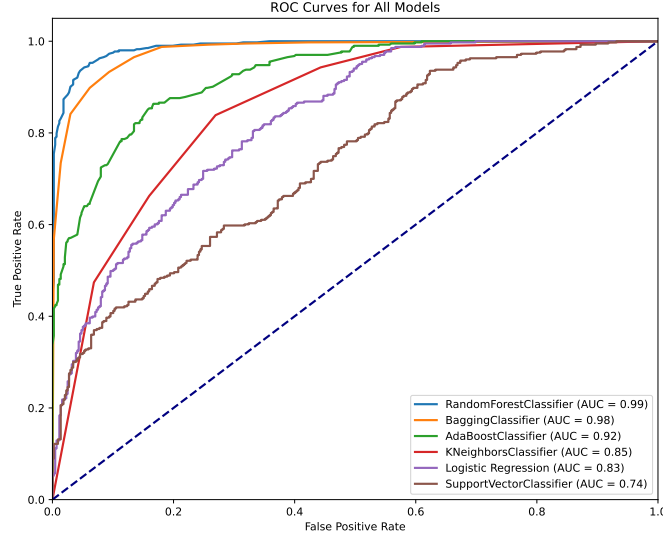


Figure 3: ROC curves for all models. The area under the curve (AUC) for each model is indicated in the legend. The dashed blue line indicates a model with an AUC of 0.5, equivalent to random guessing with no discriminatory ability.

objects. While Logistic Regression performs better than SVM, its lower accuracy and F1-scores indicate that it may not be as effective as ensemble methods for this task. However, its AUC suggests that it has a reasonable ability to distinguish between the two classes.

Finally, the *Support Vector Machine (SVM)* model achieves the lowest accuracy among the evaluated models, with an accuracy of 66% and an AUC of 0.74. Its F1-scores of 0.69 for non-lensed objects and 0.62 for lensed objects indicate that SVM may not be well-suited for this task, possibly due to the dataset’s characteristics or the model’s sensitivity to parameter tuning.

In figure 4 we present the results of our analysis for Random Forest (the best model found in this study), focusing on the light curves of selected sources from the test set. These light curves are categorized based on their true labels (Lensed or Non-Lensed) and compared with the predicted labels from our machine learning model. The results demonstrate the effectiveness of our machine learning model in classifying light curves as Lensed or Non-Lensed. As shown in Figure 4, the model correctly predicts the labels for most sources, with only a few misclassifications. For example, Source 2456

Light Curves from Test Set with True and Predicted Labels

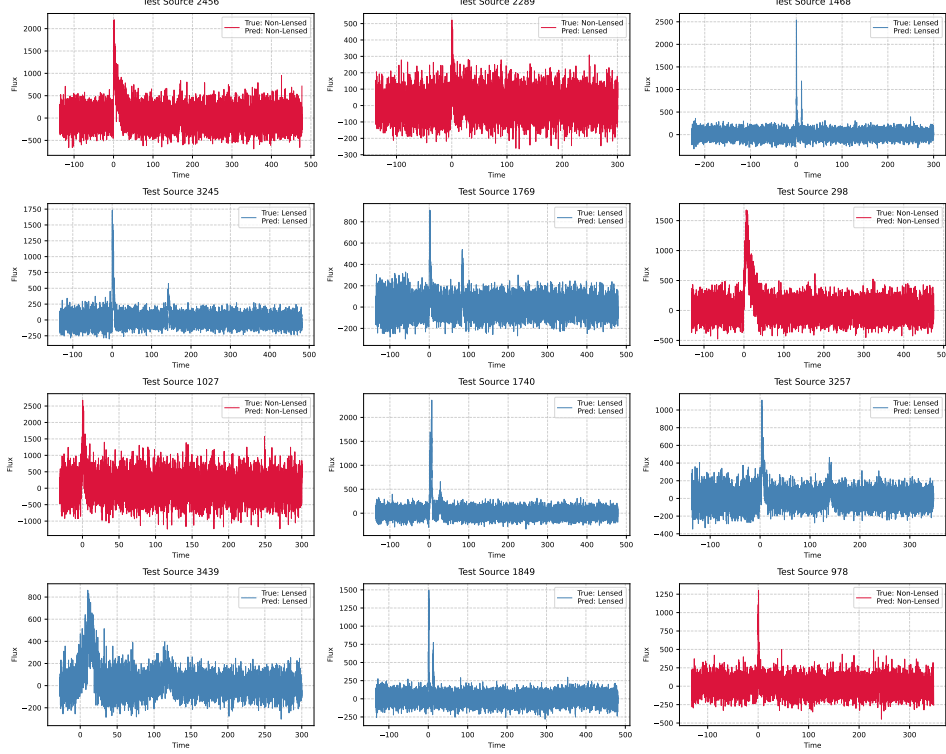


Figure 4: Light curves of selected sources from the test set. Each subplot shows the time series data for a specific source, with the true label (Lensed or Non-Lensed) and the predicted label from our machine learning model. The color coding distinguishes between Non-Lensed (red) and Lensed (blue) sources.

and Source 1468 are correctly identified as Non-lensed and Lensed, respectively, while Source 2289 shows a slight discrepancy between the true and predicted labels.

5.2 Learning Curve Analysis

To evaluate the performance and generalization capability of different classifiers, we analyzed their learning curves. Figure 5 illustrates the learning curves of AdaBoost, Logistic Regression, Support Vector Classifier (SVC), k-Nearest Neighbors (kNN), Random Forest, and Bagging classifiers. Each curve shows the training and cross-validation scores as a function of the num-

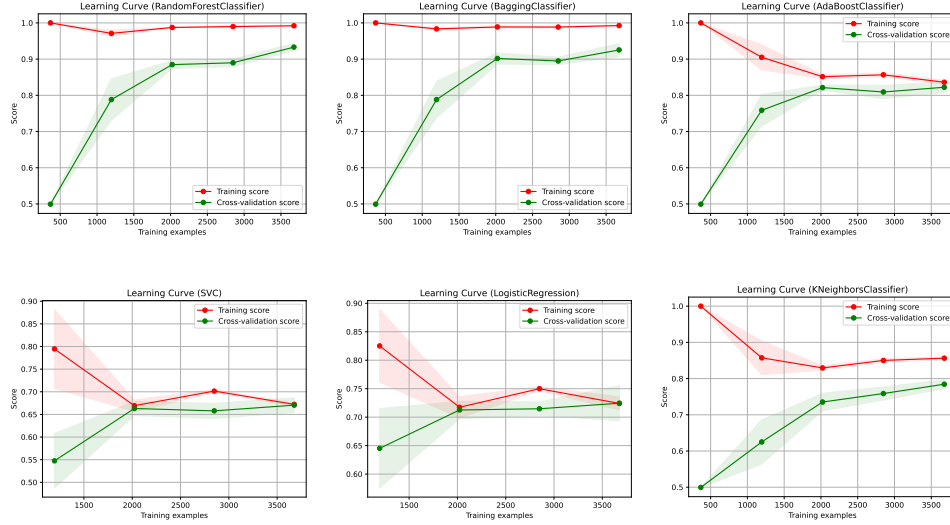


Figure 5: Learning curve for our six models. The plot shows the training and cross-validation scores as the number of training examples increases. The shaded regions around the lines represent the variance of the training and cross-validation scores across different cross-validation folds.

ber of training examples. These learning curves provide insights into how well each model learns from the data and generalizes to unseen examples.

5.2.1 Random Forest and Bagging Classifiers

Both the Random Forest and Bagging classifiers exhibit highly stable learning curves. The training score starts at 1.0, decreases slightly, and stabilizes around 0.99. The validation score, initially at 0.5, steadily increases to 0.94, demonstrating strong generalization performance. The small final gap of approximately 0.05 between training and validation scores indicates minimal overfitting, making these models the best-performing classifiers in this comparison.

5.2.2 AdaBoost Classifier

The learning curve of the AdaBoost classifier shows a strong generalization trend. The training score starts at 1.0 and gradually decreases to approx-

imately 0.84 as the number of training samples increases. Simultaneously, the cross-validation score improves from 0.5 to around 0.83, suggesting that increasing the training data effectively enhances model generalization. The relatively small final gap between training and validation scores indicates a well-balanced model with reduced overfitting.

5.2.3 k-Nearest Neighbors (kNN)

The learning curve of kNN demonstrates an interesting pattern. The training score starts at 1.0, then decreases to about 0.84 before slightly increasing again to 0.87 at the end. Meanwhile, the validation score steadily rises from 0.5 to approximately 0.79. The final gap of about 0.09 between training and validation scores suggests that kNN slightly overfits the training data, but the improvement in validation performance indicates that it benefits from additional training examples.

5.2.4 Logistic Regression

The learning curve of Logistic Regression shows a distinct trend. The training score starts at about 0.83 and decreases with more training data, reaching 0.73 at the end. The validation score, however, increases from 0.65 to approximately 0.73. The presence of fluctuations in the training curve suggests sensitivity to specific training instances, while larger error bars at the beginning and end indicate that the model is unstable. These results suggest that Logistic Regression is not a good model for microlensed GRB classification.

5.2.5 Support Vector Classifier (SVC)

The SVC learning curve follows a similar trend to Logistic Regression. The training score begins at approximately 0.8 and decreases as more data is introduced, to around 0.67. The validation score, initially at 0.55, gradually improves to 0.67. Fluctuations in the training score indicate sensitivity to sample variations, and large error bars at the beginning further confirm the instability of the model with small datasets. While SVC improves with more data, its performance remains lower than ensemble methods and the model is suffering from high bias.

5.3 Comparison of Models

Based on the learning curves, the models can be compared as follows:

Model	Non-Lensed			Lensed			Accuracy	AUC
	Precision	Recall	F1-score	Precision	Recall	F1-score		
Random Forest (RF)	0.96	0.93	0.95	0.92	0.96	0.94	94%	0.99
Bagging Classifier	0.94	0.91	0.92	0.90	0.94	0.92	92%	0.98
AdaBoostClassifier	0.84	0.86	0.85	0.84	0.82	0.83	84%	0.92
k-Nearest Neighbors (kNN)	0.83	0.73	0.78	0.74	0.84	0.79	78%	0.85
Logistic Regression	0.69	0.74	0.72	0.69	0.64	0.66	69%	0.80
Support Vector Machine (SVM)	0.65	0.73	0.69	0.66	0.58	0.62	66%	0.74

Table 1: Performance metrics for different machine learning models on the classification task. Precision, recall, and F1-score are reported for both non-lensed and Lensed classes, along with overall accuracy and AUC.

- *Best Generalization:* Random Forest and Bagging Classifier exhibit the best generalization, with small gaps between training and cross-validation scores. They are robust and perform well, showing no significant signs of underfitting or overfitting.
- *Moderate Generalization:* Logistic Regression shows good generalization, with cross-validation scores close to training scores and minimal overfitting. However, its lower training and validation scores makes it less attractive than Random Forest and Bagging Classifier for this task.
- *Overfitting and Underfitting Issues:* k-Nearest Neighbors (kNN) exhibits significant overfitting, with larger gaps between training and cross-validation scores. When it comes to and Support Vector Classifier (SVC), while there is no sign of overfitting, the low training and validation scores suggest underfitting.

5.4 Feature Importance Analysis

To identify the most influential features contributing to the classification of gravitationally Lensed and Non-lensed GRBs, we employed a Random Forest classifier with 100 trees, a maximum depth of 10, and specific constraints on node splitting to enhance generalization. After training the model on the extracted features, we computed feature importances using the Gini impurity-based ranking provided by the trained classifier.

Figure 6 presents the most significant features based on their importance scores. The most influential features include `n_epochs`, `median_absolute_deviation`, `qso_log_chi2_qsonu`, `stetson_j`, and `weighted_average`, among others. These features capture key statistical and variability properties of light

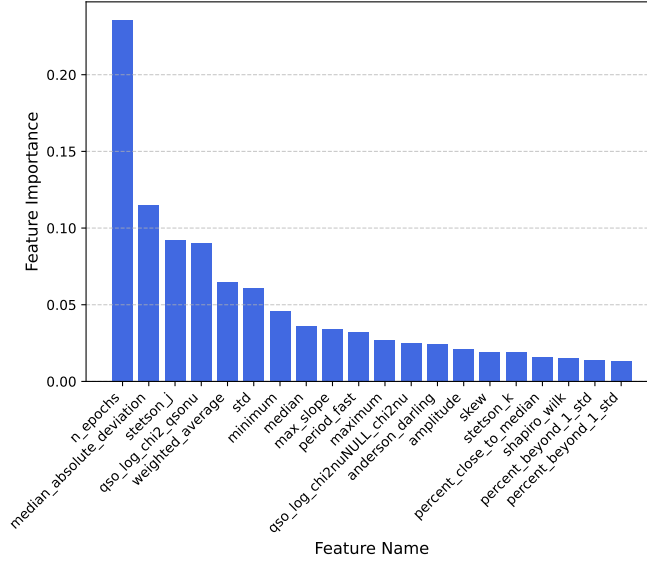


Figure 6: Top 20 most important features based on the trained Random Forest classifier. The x-axis represents the feature names, and the y-axis represents their importance scores. See section 3.2

curves, which play a crucial role in distinguishing between Lensed and Non-lensed GRBs.

The feature selection process revealed that time-series variability metrics such as `stetson_j`, `stetson_k`, and `shapiro_wilk` significantly contribute to classification performance, indicating that variability trends are pivotal in recognizing gravitational lensing signatures. Additionally, statistical descriptors like `median_absolute_deviation` and `skew` provide insights into the distributional properties of the light curves, further reinforcing their relevance to the classification task.

6 Summary and Conclusions

We investigated the possibility of classifying micro Lensed and Non-Lensed GRBs through application of some popular machine learning models. The method turned out to be successful and can be applicable for real time observations. Overall, the results demonstrate that ensemble methods such as Random Forest and Bagging Classifier are the most effective for this classification task, achieving high accuracy and balanced performance across both

classes, and exceptional AUC values. In contrast, models like SVC and kNN struggle to generalize well, highlighting the importance of model selection for this problem. The AUC metric further reinforces the superiority of ensemble methods, as they exhibit the highest ability to distinguish between Lensed and Non-lensed objects.

Additionally, analysing the learning curve of the six models demonstrate that the Random Forest and Bagging classifiers demonstrate the best trade-off between training and validation performance, with minimal overfitting and the highest validation scores. AdaBoost also generalizes well but has a less satisfactory validation score. Logistic Regression and SVC show a steady improvement in validation performance, though their lower final scores and fluctuations suggest they may not be the best choices for this dataset. The kNN classifier, while improving with additional data, exhibits signs of overfitting and remains slightly behind the ensemble methods in performance.

References

- [1] Ayubinia, A., Woo, J.-H., Hafezianzadeh, F., Kim, T., & Kim, C. 2025, *ApJ*, 980, 177, doi: 10.3847/1538-4357/ada366
- [2] Baron, D. 2019, arXiv e-prints, arXiv:1904.07248, doi: 10.48550/arXiv.1904.07248
- [3] Bradley, A. P. 1997, *Pattern Recognit.*, 30, 1145, doi: 10.1016/S0031-3203(96)00142-2
- [4] Breiman, L. 1996, *Machine Learning*, 24, 123
- [5] —. 2001, *Machine Learning*, 45, 5
- [6] Cesium Development Team. 2019, Cesium: A Python Library for Time-Series Feature Extraction, Astrophysics Source Code Library
- [7] Cortes, C., & Vapnik, V. 1995, *Machine Learning*, 20, 273
- [8] Cover, T., & Hart, P. 1967, *IEEE Transactions on Information Theory*, 13, 21
- [9] Fawcett, T. 2006, *Pattern Recognit. Lett.*, 27, 861, doi: 10.1016/j.patrec.2005.10.010
- [10] Feigelson, E. D., & Babu, G. J. 2012, *Modern Statistical Methods for Astronomy with R Applications* (Cambridge University Press)

- [11] Freund, Y., & Schapire, R. E. 1997, *Journal of Computer and System Sciences*, 55, 119
- [12] Hastie, T., Tibshirani, R., & Friedman, J. 2009, *The Elements of Statistical Learning: Data Mining, Inference, and Prediction*, 2nd edn. (New York, NY: Springer), doi: 10.1007/978-0-387-84858-7
- [13] Hirose, Y., Umemura, M., & et al. 2006, *The Astrophysical Journal*, 650
- [14] Ji, L., Kovetz, E., & et al. 2018, *Physical Review D*, 98, 123523
- [15] Kalantari, Z., Ibrahim, A., Reza Rahimi Tabar, M., & Rahvar, S. 2021, *ApJ*, 922, 77, doi: 10.3847/1538-4357/ac1c06
- [16] Kalantari, Z., & Rahvar, S. 2025, *The Astrophysical Journal*. <https://api.semanticscholar.org/CorpusID:276380524>
- [17] Kalantari, Z., Rahvar, S., & Ibrahim, A. 2022, *ApJ*, 934, 106, doi: 10.3847/1538-4357/ac7da9
- [18] Krumpe, M., Böhringer, H., Mullis, C. R., Schuecker, P., & Carey, S. R. 2007, *ApJS*, 173, 619, doi: 10.1086/522375
- [19] Kumar, P., & Zhang, B. 2015, *Physics Reports*, 561, 1, doi: 10.1016/j.physrep.2014.09.008
- [20] Lochner, M., McEwen, J. D., Peiris, H. V., Pierel, J., & Poznanski, D. 2016, *ApJS*, 225, 31, doi: 10.3847/0067-0049/225/2/31
- [21] MacLeod, C. L., Ivezić, Ž., Kochanek, C. S., et al. 2010, *The Astrophysical Journal*, 721, 1014
- [22] Mao, S. 1992, *Astrophysical Journal*, Part 2, 389, L41
- [23] Meegan, C., Lichti, G., & et al. 2009, *The Astrophysical Journal*, 702, 791–804
- [24] Mészáros, P. 2006, *Reports on Progress in Physics*, 69, 2259, doi: 10.1088/0034-4885/69/8/R01
- [25] Möller, A., & de Boissière, T. 2020, *MNRAS*, 491, 4277, doi: 10.1093/mnras/stz3241
- [26] Naul, B., Bloom, J. S., Perez, F., & Van Der Walt, S. 2018, *AJ*, 156, 1, doi: 10.3847/1538-3881/aae645

- [27] Oguri, M. 2019, Reports on Progress in Physics, 82, 126901, doi: 10.1088/1361-6633/ab4fc5
- [28] —. 2019, Reports on Progress in Physics, 82, 126901
- [29] Ougolnikov, O. 2003, Cosmic Research, 41, 141
- [30] Paczynski, B. 1986, Astrophysical Journal, Part 2 - Letters to the Editor (ISSN 0004-637X), 308, L43
- [31] Powers, D. M. 2011, J. Mach. Learn. Technol., 2, 37
- [32] Richards, J. W., Starr, D. L., Miller, A. A., et al. 2011, ApJ, 733, 10, doi: 10.1088/0004-637X/733/1/10
- [33] Richards, J. W., Starr, D. L., Butler, N. R., et al. 2011, The Astrophysical Journal, 733, 10
- [34] Saito, T., & Rehmsmeier, M. 2015, PLoS One, 10, e0118432, doi: 10.1371/journal.pone.0118432
- [35] Stetson, P. B. 1996, Publications of the Astronomical Society of the Pacific, 108, 851
- [36] von Kienlin, A., Meegan, C. A., Paciesas, W. S., et al. 2020, apj, 893, 46, doi: 10.3847/1538-4357/ab7a18
- [37] Wang, J., Zhang, C., Liu, Z., Wang, J., & Wu, X. 2020, MNRAS, 491, 2018, doi: 10.1093/mnras/stz3067
- [38] Wang, Y., Zhang, S.-R., Momtaz, A., et al. 2024, arXiv e-prints, arXiv:2404.10019, doi: 10.48550/arXiv.2404.10019
- [39] Zhang, B. B., Zhang, B., & Liang, E. W. 2009, ApJL, 703, L162, doi: 10.1088/0004-637X/703/2/L162
- [40] Zhoolideh Haghighi, M. H., Ghasrimanesh, A., & Khosroshahi, H. 2025, Machine Learning with Applications, 20, 100640, doi: <https://doi.org/10.1016/j.mlwa.2025.100640>
- [41] Zhoolideh Haghighi, M. H. Z. 2023, Astronomical and Astrophysical Transactions, 33, 323, doi: <https://aaptr.com/articles/7534>